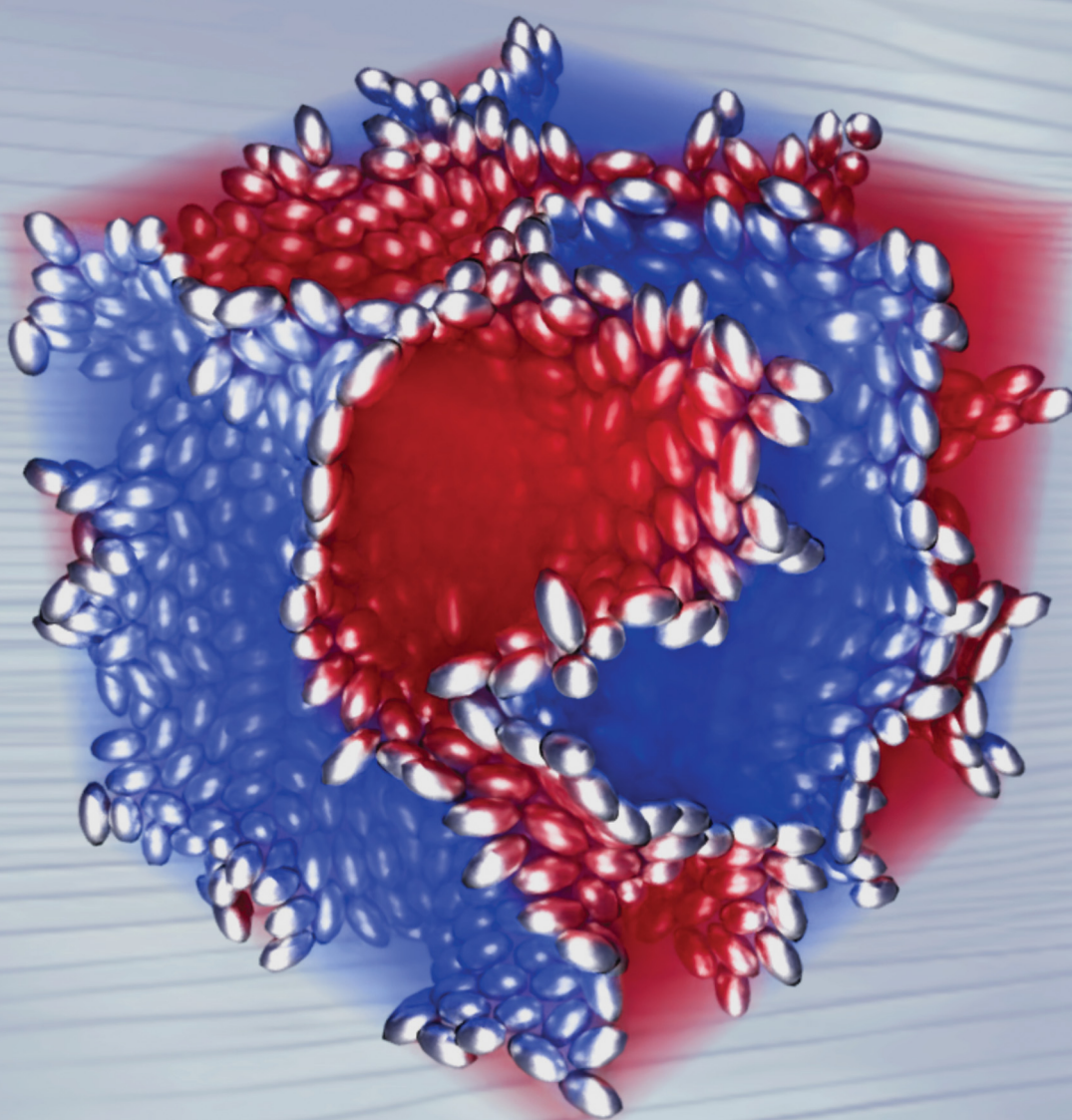


Soft Matter

rsc.li/soft-matter-journal



ISSN 1744-6848



Cite this: *Soft Matter*, 2024,
20, 8952

Formation of bijels stabilized by magnetic ellipsoidal particles in external magnetic fields

Nikhil Karthikeyan ^b and Ulf D. Schiller ^{*ab}

Bicontinuous interfacially-jammed emulsion gels (bijels) are increasingly used as emulsion templates for the fabrication of functional porous materials including membranes, electrodes, and biomaterials. Control over the domain size and structure is highly desirable in these applications. For bijels stabilized by spherical particles, particle size and volume fraction are the main parameters that determine the emulsion structure. Here, we investigate the use of ellipsoidal magnetic particles and study the effect of external magnetic fields on the formation of bijels. Using hybrid Lattice Boltzmann-molecular dynamics simulations, we analyze the effect of the magnetic field on emulsion dynamics and the structural properties of the resulting bijel. We find that the formation of bijels remains robust in the presence of magnetic fields, and that the domain size and tortuosity become anisotropic when ellipsoidal particles are used. We show that the magnetic fields lead to orientational ordering of the particles which in turn leads to alignment of the interfaces. The orientational order facilitates enhanced packing of particles in the interface which leads to different jamming times in the directions parallel and perpendicular to the field. Our results highlight the potential of magnetic particles for fabrication and processing of emulsion systems with tunable properties.

Received 19th June 2024,
Accepted 4th October 2024

DOI: 10.1039/d4sm00751d

rsc.li/soft-matter-journal

1 Introduction

Mixtures of two or more immiscible liquids commonly form emulsions whose structures can serve as templates for fabrication of porous materials, including porous polymers,^{1,2} porous ceramics,^{3,4} synthetic nanoparticles,⁵ and artificial tissue.⁶ Emulsion templating provides a facile route to tailoring the properties of porous materials by leveraging processing techniques that offer control over the volume fraction, domain size, and composition of the emulsion.⁷ Thermodynamic and mechanical stability are essential for processing of emulsion templates, and particle-stabilization has emerged as a viable alternative to surfactant-stabilization while avoiding potentially harmful chemicals. Emulsions stabilized by particles are commonly known as Pickering emulsions,^{8,9} and a variety of particle types have been used to stabilize emulsions, ranging from polystyrene colloidal particles¹⁰ to carbon nanotubes (CNTs).¹¹

Bicontinuous interfacially stabilized emulsion gels (bijels) are a particular class of particle-stabilized emulsions with a bicontinuous domain morphology.¹² Bijels emerge when a binary mixture containing particles is quenched rapidly into

the phase separating region. Spinodal decomposition leads to formation of large interfaces that sequester the particles while sweeping through the system. During coarsening of the phases, the particles become jammed and arrest the phase-separation, locking in the bicontinuous phase morphology. Bijels were first discovered in simulations¹³ and subsequently realized in water-lutidine mixtures with silica particles.^{14,15} A range of robust and versatile formulations of bijels have since been developed.^{16–18} For example, Haase *et al.*¹⁹ used solvent transfer-induced phase separation (STRIPS) as a versatile and scalable technique that combines separation with an imposed flow that offers control over the formation of droplets and jets. Following these fundamental developments, bijels have gained popularity as emulsion templates for the fabrication of functional porous materials including membranes,^{19–21} electrodes,^{22,23} and biomaterials.^{6,24,25}

Anisotropic particles, when adsorbed at liquid interfaces, induce shape-dependent capillary interactions that can have a distinct effect on the microstructure of emulsions.^{26,27} For instance, Madivala *et al.*^{28,29} found that emulsion stability can be significantly enhanced by ellipsoidal particles. Additionally, capillary interactions can lead to direct assembly of anisotropic particles.^{30–33} Ellipsoidal particles can rotate and migrate on curved surfaces,³⁴ where the interface curvature acts as an external field that controls the orientation and placement of particles.³⁵ Anisotropic particles at fluid interfaces were considered in Monte Carlo simulations by Bresme *et al.* to test the

^a Department of Computer and Information Sciences, University of Delaware, Newark, DE 19716, USA. E-mail: uschill@udel.edu

^b Department of Materials Science and Engineering, University of Delaware, Newark, DE 19716, USA



accuracy of thermodynamic models for the free energy as a function of the particle–fluid interactions, particle size, and orientation.^{36,37} Harting and co-workers^{38,39} have performed lattice Boltzmann simulations of anisotropic particles at liquid interfaces and in emulsions. They found that anisotropic particles affect the dynamics of emulsion formation by introducing two additional timescales associated with particle rotation. Following initial adsorption, particles rotate to align their larger cross-section with the interface. When jamming sets in, capillary interactions cause the particle to re-orient in the interface leading to prolonged coarsening at long timescales. Due to the larger aspect ratio, ellipsoidal particles can stabilize a larger interface area leading to smaller domain sizes. Huijnen *et al.*⁴⁰ experimentally realized bijels stabilized by colloidal rods and analyzed their effect on the interface and domain morphology. Their experiments confirmed that jamming occurs at lower interface separations than for spherical particles with the same volume fraction. Moreover, they observed that the overall structure remains isotropic and attributed this to the rapid jamming of the rods. Additionally, they found that some rods tilted out of the interface due to the compression induced by domain coarsening.

Particle-stabilized emulsions can be made responsive to external magnetic fields by magnetic particles.^{41,42} An external field can then be used to control the stability of the emulsion⁴¹ and the self-assembly of particles.^{43,44} The tendency of anisotropic particles to adopt distinct orientations gives rise to an orientation transition when an external field is applied.^{45–47} Magnetic fields thus offer a means to control the capillary interactions of ellipsoidal particles at an interface. For bijels stabilized by spherical magnetic particles, simulations by Kim *et al.*⁴⁸ revealed that magnetic fields do not have a significant effect on the microstructure of bijels. In contrast, Carmack and Millett⁴⁹ demonstrated that the structure of thin-film bijels stabilized by dielectric particles can change drastically when an external electric field is applied. The dielectric contrast of the particles induces polar interactions that cause liquid domain alignment leading to percolating cylindrical domains in the thin-film bijel. In addition, they found that particle chains can act as nucleation sites for phase separation. This suggests that anisotropic interactions can have a considerable effect on the phase separation and the resulting emulsion morphology and may offer a means to control the size and shape of liquid domains.

In this work, we investigate the effect of external magnetic fields on the formation of bijels stabilized by anisotropic magnetic particles. We performed hybrid Lattice Boltzmann–molecular dynamics simulations of a binary liquid with suspended anisotropic particles that possess a permanent magnetic dipole moment along their symmetry axis. We analyzed the structural properties of bijels that form with oblate, spherical, and prolate particles in magnetic fields at different flux densities. The results show that, while the overall bijel formation is not disrupted by the magnetic field, the resulting domain morphology varies depending on the particle aspect ratio and the magnetic flux density. Notably, the average

domain spacing and tortuosity of the bijel become anisotropic. Analysis of the orientational order reveals that the kinetic formation of the bijel is governed by rotation of particles due to the magnetic field, which in turn causes a re-alignment of the liquid domains. The increased orientational order within the interfaces facilitates particle packing and delays the onset of jamming. The resulting interfacial particle arrangement exhibits a higher degree of structural order compared with bijels formed in the absence of a magnetic field. These results demonstrate the potential of magnetic particles in fabricating emulsion systems with tunable domain structure.

2 Methods

2.1 Lattice Boltzmann method for binary mixture

We employed a multicomponent lattice Boltzmann model to simulate an immiscible binary fluid. In the multicomponent lattice Boltzmann method,^{50–52} each fluid component k is represented by populations $f_i^k(\mathbf{x}, t)$ that evolve in discrete time-steps Δt on a cubic lattice with lattice spacing Δx . The populations f_i^k are associated with discrete velocities \mathbf{c}_i such that $\mathbf{c}_i \Delta t$ connects the lattice sites, and $f_i^k(\mathbf{x}, t)$ represents the density of fluid k at lattice site \mathbf{x} and time t that is moving with velocity \mathbf{c}_i . In this work, we use the D3Q19 velocity set⁵³ that connects nearest and next-nearest neighbors on the lattice and includes a rest population f_0^k associated with $\mathbf{c}_0 = 0$. The evolution of the populations is governed by the lattice Boltzmann equation with a BGK collision term⁵⁴

$$f_i^k(\mathbf{x} + \mathbf{c}_i \Delta t, t + \Delta t) = f_i^k(\mathbf{x}, t) - \frac{\Delta t}{\tau_k} [f_i^k(\mathbf{x}, t) - f_i^{k, \text{eq}}(\rho_k, \mathbf{u}_k^{\text{eq}})], \quad (1)$$

where $f_i^{k, \text{eq}}(\rho_k, \mathbf{u}_k^{\text{eq}})$ denotes an equilibrium distribution that depends on the local fluid density $\rho_k = \sum_k f_i^k$ and velocity \mathbf{u}_k^{eq} (specified below). The equilibrium distribution $f_i^{k, \text{eq}} = f_i^{\text{eq}}$ is written as a polynomial expansion in the velocity

$$f_i^{\text{eq}}(\rho, \mathbf{u}) = w_i \rho \left(1 + \frac{\mathbf{c}_i \cdot \mathbf{u}}{c_s^2} + \frac{(\mathbf{c}_i \mathbf{c}_i - c_s^2 \mathbf{1}) : \mathbf{u} \mathbf{u}}{2c_s^4} \right), \quad (2)$$

where $w_i = w_{|\mathbf{c}_i|}$ are lattice weights and c_s is the (pseudo-)speed of sound. For the D3Q19 model, the weights are $w_{|\mathbf{c}_i|=0} = \frac{1}{3}$, $w_{|\mathbf{c}_i|=1} = \frac{1}{18}$, $w_{|\mathbf{c}_i|=\sqrt{2}} = \frac{1}{36}$, and the speed of sound is $c_s = \frac{1}{\sqrt{3}} \frac{\Delta x}{\Delta t}$.

To incorporate nonideal interactions, we adopt the Shan–Chen model^{50,55} and introduce momentum transfer between the fluid components in terms of a non-local interaction force

$$\mathbf{F}_k(\mathbf{x}) \Delta t = - \sum_{k'} \sum_i \frac{w_i}{c_s^2} g_{kk'} \psi_k(\mathbf{x}) \psi_{k'}(\mathbf{x} + \mathbf{c}_i) \mathbf{c}_i, \quad (3)$$

where $\psi_k(\mathbf{x}) = \psi(\rho_k(\mathbf{x}))$ represents the effective density of the



fluid component k taken as the function

$$\psi(\rho) = \rho_0 \left[1 - \exp\left(-\frac{\rho}{\rho_0}\right) \right] \quad (4)$$

with a reference density ρ_0 . The momentum change caused by the force is incorporated in the lattice Boltzmann equation by defining the velocity to be used in the calculation of the equilibrium distribution $f_i^{k,\text{eq}}$ as

$$\mathbf{u}_k^{\text{eq}} = \mathbf{u}' + \frac{\tau_k}{\rho_k} \mathbf{F}_k. \quad (5)$$

The common velocity \mathbf{u}' is defined through

$$\sum_k \frac{\rho_k}{\tau_k} \mathbf{u}' = \sum_k \frac{1}{\tau_k} \sum_i f_i^k \mathbf{c}_i \quad (6)$$

which ensures that in the absence of forces, the total momentum of all components is conserved. The total mass density and momentum of the fluid are given by⁵¹

$$\begin{aligned} \rho &= \sum_k \rho_k = \sum_k \sum_i f_i^k, \\ \rho \mathbf{u} &= \sum_k \sum_i f_i^k \mathbf{c}_i + \frac{\Delta t}{2} \sum_k \mathbf{F}_k. \end{aligned} \quad (7)$$

The macroscopic transport equations can be obtained by carrying out a Chapman–Enskog expansion. For the multi-component model introduced above, it yields the mass and momentum equation for the binary fluid mixture^{51,56}

$$\begin{aligned} \frac{\partial \rho}{\partial t} + \nabla \cdot (\rho \mathbf{u}) &= 0, \\ \frac{\partial \mathbf{u}}{\partial t} + (\mathbf{u} \cdot \nabla) \mathbf{u} &= -\frac{1}{\rho} \nabla p + \nu \nabla^2 \mathbf{u}, \end{aligned} \quad (8)$$

where the pressure p is given by the nonideal equation of state

$$p = \rho c_s^2 + \frac{1}{2} \sum_{k,k'} g_{kk'} \psi_k \psi_{k'}, \quad (9)$$

and the kinematic viscosity of the fluid is given by

$$\nu = c_s^2 \left(\sum_k \frac{\rho_k}{\rho} \tau_k - \frac{1}{2} \right). \quad (10)$$

In a binary fluid, the density profile of the components can be described by a single order parameter $\phi = \frac{\rho_k - \rho_{k^*}}{\rho_k + \rho_{k^*}}$ that is governed by a diffusion equation. For an incompressible fluid, we have $\nabla \rho_{k^*} = -\nabla \rho_k = \frac{\rho}{2} \nabla \phi$. In this work, we use equal relaxation times $\tau = \tau_k = \tau_{k^*}$ for both fluids. We also set the self-interactions to zero $g_{kk} = g_{k^*k^*} = 0$ and use a single interaction parameter $g = g_{kk^*} = g_{k^*k}$. The diffusion equation for the order parameter simplifies to⁵⁰

$$\frac{\partial \phi}{\partial t} + \nabla \cdot (\phi \mathbf{u}) = \nabla \cdot (\Gamma \nabla \phi) \quad (11)$$

with an order parameter diffusivity

$$\Gamma = c_s^2 \left(\tau - \frac{1}{2} \right) - \tau g \frac{\rho_{k^*} \psi_k \psi'_k + \rho_k \psi_{k^*} \psi'_{k^*}}{\rho}. \quad (12)$$

In addition to a non-ideal equation of state, the Shan–Chen force also leads to a surface tension at the interface between two immiscible components. The surface tension σ depends on the interaction parameters g_{kk^*} and can formally be obtained from the full pressure tensor \mathbf{P} by integrating over a planar interface^{55,57}

$$\sigma = \int_{-\infty}^{\infty} (P_{zz} - P_{xx}) dz. \quad (13)$$

In practice, it is common to determine the value of σ for a chosen g_{kk^*} by performing a simulation of a spherical droplet and using the Young–Laplace equation to calculate the surface tension from the measured droplet radius and pressure drop across its interface. We have taken this route and report the measured surface tension in Section 2.2.4.

2.2 Suspended colloidal particles

Suspended particles can be coupled to the lattice Boltzmann fluid by the approach pioneered by Ladd^{58–61} and Aidun.⁶² The particles are assumed to be rigid bodies that evolve according to Newton's equation of motion

$$\begin{aligned} \mathbf{F}_p &= m_p \frac{\mathbf{u}_p}{dt}, \\ \mathbf{D}_p &= J_p \frac{\mathbf{w}_p}{dt}, \end{aligned} \quad (14)$$

where F_p and D_p are the force and torque acting on the particle, \mathbf{u}_p and ω_p are the linear and angular velocity, and m_p and J_p the mass and moment of inertia. Eqn (14) can be solved using a standard MD integrator.⁶³ To couple the particles to the LB fluid, the particles are overlayed on the lattice, and sites covered by the particle are marked as solid nodes. LB populations that move along velocities connecting fluid and solid nodes are updated according to a moving bounce-back boundary condition, *i.e.*, if \mathbf{x} is a fluid node and $\mathbf{x} + \mathbf{c}_i \Delta t$ is a solid node, the propagation step is modified to

$$f_{i*}^k(\mathbf{x}, t + \Delta t) = f_i^{k,*}(\mathbf{x}, t) - \frac{2w_i}{c_s^2} \rho \mathbf{u}_i \cdot \mathbf{c}_i, \quad (15)$$

where $\mathbf{c}_i = -\mathbf{c}_i$ and $f_i^{k,*}(\mathbf{x}, t)$ is the post-collision population, and $\mathbf{u}_i = \mathbf{u}_p + \omega \times \mathbf{r}_i$ is the velocity of the particle surface at $\mathbf{r}_i = \mathbf{x} + \frac{\Delta t}{2} \mathbf{c}_i - \mathbf{R}_{\text{cms}}$ with \mathbf{R}_{cms} the particle's center of mass. The momentum change $\Delta \mathbf{p}_i^k \frac{\Delta t}{(\Delta x)^3} = 2f_i^{k,*}(\mathbf{x}, t) \mathbf{c}_i - \frac{2w_i}{c_s^2} \rho (\mathbf{u}_i \cdot \mathbf{c}_i) \mathbf{c}_i$ associated with the bounce-back of both fluid components is summed over the surface of the particle to obtain the force and



torque on the particle

$$\mathbf{F}_p = \sum_{k,i} \frac{\Delta \mathbf{p}_i^k}{\Delta t}, \quad (16)$$

$$\mathbf{T}_p = \sum_{k,i} \frac{\Delta \mathbf{p}_i^k}{\Delta t} \times \mathbf{r}_i.$$

As the particle moves over the lattice, it covers and uncovers individual lattice sites which then turn from fluid into solid nodes and *vice versa*. When a lattice site \mathbf{x} becomes covered, its momentum is transferred to the particle by a force

$$\mathbf{F}_p = - \sum_{k,i} f_i^k(\mathbf{x}, t) \mathbf{c}_i. \quad (17)$$

When a lattice site \mathbf{x} becomes uncovered, it is filled with the average density of N_f neighboring fluid nodes at $\mathbf{x} + \mathbf{c}_i$

$$\rho^k(\mathbf{x}, t) = \frac{1}{N_f} \sum_{i_f} \rho^k(\mathbf{x} + \mathbf{c}_{i_f}, t). \quad (18)$$

To evaluate the Shan–Chen force (3) at particle surfaces, we use the same expression for assigning a virtual density $\rho_v^k(\mathbf{x}, t)$ to the outer shell of solid nodes inside the particle. An additional shift $\Delta \rho$ in the density of either fluid component can be imposed to control the fluid contact angle at the particle surface.^{64,65}

2.2.1 Particles near contact. For particles close to contact, we add a lubrication force to account for the unresolved hydrodynamics. The lubrication correction is added to particle pairs that are separated by a gap d smaller than a cutoff d_c and is given as^{61,66}

$$\mathbf{F}_l = -6\pi\eta \frac{R_1^2 R_2^2}{(R_1 + R_2)^2} \left(\frac{1}{|\mathbf{r}_{ij}| - R_1 - R_2} - \frac{1}{d_c} \right) \frac{(\mathbf{u}_{12} \cdot \mathbf{r}_{12}) \mathbf{r}_{12}}{|\mathbf{r}_{12}|^2}, \quad (19)$$

where $\mathbf{u}_{12} = \mathbf{u}_1 - \mathbf{u}_2$ is the relative velocity, \mathbf{r}_{12} is the vector connecting the centers of the particles, and $d = |\mathbf{r}_{12}| - R_1 - R_2$ is the gap between the particle surfaces with curvature radii R_1 and R_2 . Despite the repulsive nature of the lubrication forces, particle overlaps can still occur in numerical simulations. To address the possibility of particle contact and overlap, we add a Hertz force $\mathbf{F}_H = -\nabla\phi_H$ to the particle–particle interactions, which is derived from the Hertz potential

$$\phi_H(\mathbf{r}_{12}) = K_H (R_1 + R_2 - |\mathbf{r}_{12}|)^{\frac{5}{2}}, \quad |\mathbf{r}_{12}| < R_1 + R_2. \quad (20)$$

2.2.2 Anisotropic particles. The interparticle forces (19) and (20) can be generalized for ellipsoidal particles following Günther *et al.*^{38,39} who adopted an approach proposed by Berne *et al.*^{67,68} We first rescale the potential and force such that

$$\phi(\mathbf{r}_{ij}) = \varepsilon \tilde{\phi}\left(\frac{\mathbf{r}_{ij}}{\sigma}\right), \quad (21)$$

$$\mathbf{F}(\mathbf{r}_{ij}) = \varepsilon \tilde{\mathbf{F}}\left(\frac{\mathbf{r}_{ij}}{\sigma}\right).$$

For the lubrication force (19), we choose $\sigma = R_1 + R_2$ and $\varepsilon = \frac{6\pi\eta R_1^2 R_2^2}{\sigma^3}$, and for the Hertz potential we chose $\sigma = R_1 + R_2$

and $\varepsilon = K_H \sigma^{5/2}$. For two identical, rotationally symmetric ellipsoidal particles with orientations $\hat{\mathbf{o}}_i$ and $\hat{\mathbf{o}}_j$, we then replace ε and σ by the anisotropic functions

$$\tilde{\varepsilon}(\hat{\mathbf{o}}_i, \hat{\mathbf{o}}_j) = \frac{\varepsilon}{\sqrt{1 - \chi^2}},$$

$$\tilde{\sigma}(\mathbf{r}_{ij}, \hat{\mathbf{o}}_i, \hat{\mathbf{o}}_j) = \frac{\sigma}{\sqrt{1 - \frac{\chi}{2} \left[\frac{(\hat{\mathbf{r}}_{ij} \cdot \hat{\mathbf{o}}_i + \hat{\mathbf{r}}_{ij} \cdot \hat{\mathbf{o}}_j)^2}{1 + \chi(\hat{\mathbf{o}}_i \cdot \hat{\mathbf{o}}_j)} + \frac{(\hat{\mathbf{r}}_{ij} \cdot \hat{\mathbf{o}}_i - \hat{\mathbf{r}}_{ij} \cdot \hat{\mathbf{o}}_j)^2}{1 - \chi(\hat{\mathbf{o}}_i \cdot \hat{\mathbf{o}}_j)} \right]}},$$

$$\chi = \frac{\alpha^2 - 1}{\alpha^2 + 1}, \quad (22)$$

where R_{\parallel} is the particle radius along the symmetry axis $\hat{\mathbf{o}}$ and $\alpha = R_{\parallel}/R_{\perp}$ the aspect ratio of the particle. The anisotropic Hertz potential and lubrication force are then defined as

$$\phi(\mathbf{r}_{ij}, \hat{\mathbf{o}}_i, \hat{\mathbf{o}}_j) = \varepsilon(\hat{\mathbf{o}}_i, \hat{\mathbf{o}}_j) \tilde{\phi}\left(\frac{\mathbf{r}_{ij}}{\sigma(\mathbf{r}_{ij}, \hat{\mathbf{o}}_i, \hat{\mathbf{o}}_j)}\right), \quad (23)$$

$$\mathbf{F}(\mathbf{r}_{ij}, \hat{\mathbf{o}}_i, \hat{\mathbf{o}}_j) = \varepsilon(\hat{\mathbf{o}}_i, \hat{\mathbf{o}}_j) \tilde{\mathbf{F}}\left(\frac{\mathbf{r}_{ij}}{\sigma(\mathbf{r}_{ij}, \hat{\mathbf{o}}_i, \hat{\mathbf{o}}_j)}\right).$$

2.2.3 Magnetic particles and magnetic fields. Particles with a constant magnetic dipole moment $\mathbf{m} = m\hat{\mathbf{o}}$ have been considered by Harting and coworkers.^{46,69–71} The interaction between magnetic particles is modeled by the pairwise potential between two dipoles \mathbf{m}_i and \mathbf{m}_j that are separated in space by a vector \mathbf{r}_{ij}

$$U(\mathbf{r}_{ij}, \mathbf{m}_i, \mathbf{m}_j) = \frac{\mu_0}{4\pi} \left[\frac{\mathbf{m}_i \cdot \mathbf{m}_j}{|\mathbf{r}_{ij}|^3} - \frac{3(\mathbf{m}_i \cdot \mathbf{r}_{ij})(\mathbf{m}_j \cdot \mathbf{r}_{ij})}{|\mathbf{r}_{ij}|^5} \right], \quad (24)$$

where μ_0 is the vacuum permeability. The dipole–dipole force and torque exerted by particle j on particle i are thus

$$\mathbf{F}_{ij} = \frac{3\mu_0}{4\pi} \left[\frac{5(\mathbf{m}_i \cdot \mathbf{r}_{ij})(\mathbf{m}_j \cdot \mathbf{r}_{ij})}{|\mathbf{r}_{ij}|^7} \mathbf{r}_{ij} - \frac{(\mathbf{m}_i \cdot \mathbf{m}_j)\mathbf{r}_{ij} + (\mathbf{m}_i \cdot \mathbf{r}_{ij})\mathbf{m}_i + (\mathbf{m}_i \cdot \mathbf{r}_{ij})\mathbf{m}_j}{|\mathbf{r}_{ij}|^5} \right], \quad (25)$$

$$\mathbf{T}_{ij} = \frac{\mu_0}{4\pi} \left[\frac{3(\mathbf{m}_j \cdot \mathbf{r}_{ij})\mathbf{m}_i \times \mathbf{r}_{ij}}{|\mathbf{r}_{ij}|^5} - \frac{\mathbf{m}_i \times \mathbf{m}_j}{|\mathbf{r}_{ij}|^3} \right].$$

Here it is assumed that the dipole moment of the particles does not change in an external field and that it is oriented along the symmetry axis of ellipsoidal particles, as was observed experimentally in ref. 72 and 73 (*cf.* Section 2.2.4).

An external magnetic flux density $\mathbf{B} = \mu_0 \mathbf{H}$ exerts a force and a torque on each dipole

$$\mathbf{F}_i = (\mathbf{m}_i \cdot \nabla) \mathbf{B},$$

$$\mathbf{T}_i = \mathbf{m}_i \times \mathbf{B}. \quad (26)$$



The total magnetic force and torque exerted on the particles are the sums of the dipole–dipole and field contributions.

2.2.4 Model parameters and simulation setup. The dynamics of the binary fluid mixture is governed by inertial, viscous, and surface tension forces. The relative magnitudes of these forces at a characteristic length scale L and characteristic velocity U are captured by the capillary number $\text{Ca} = \frac{\eta U}{\sigma}$ and

the Weber number $\text{We} = \frac{\rho U^2 L}{\sigma}$. Here we are primarily interested in spinodal decomposition of the mixture, where we analyze the dynamics after the initial formation of the interfaces and neglect residual diffusion. Hence the Peclet number $\text{Pe} = \frac{UL}{\Gamma}$ is of lesser importance and we do not consider it when choosing our simulation parameters.

The equations of motion of our model comprise the relevant materials properties: the density ρ , viscosity ν , and surface tension σ of the binary fluid, and the mass m_p , size R_p and aspect ratio α , and dipole moment m of the particles. In addition, we can control the particle volume fraction ϕ_p and magnetic field strength B . These nine quantities involve four unit dimensions (mass, length, time, and charge), hence we can use five dimensionless variables to specify the parameters of the system. These are the particle aspect ratio α , particle volume fraction ϕ_p , particle *vs.* fluid density ratio $\xi = 3m_p/(4\pi\rho V_p)$, nominal Weber number $\text{We}_n = \rho\sigma V_p^{1/3}/\eta^2$, and magnetic Bond number $\bar{B} = mB/(\sigma A_p)$, where $V_p = (4/3)\pi R_{\parallel}^3/\alpha^2$ is the particle volume and $A_p = \max(\pi R_{\parallel}^2/\alpha, \pi R_{\parallel}^2/\alpha^2)$ the area of the larger cross-section of the ellipsoidal particles.

For our simulations, we choose units Δx , Δt , Δm , and Δi such that $V_p = \hat{V}_p(\Delta x)^3$, $\nu = \hat{\nu}(\Delta x)^2/\Delta t$, $\sigma = \hat{\sigma}\Delta m/(\Delta t)^2$, and $m = \hat{m}\Delta i(\Delta x)^2$. We used $V_p = 2000\pi/3$, $\hat{\nu} = 1/6$, $\hat{\sigma} = 0.0267$, $\hat{m} = 1$, and a density ratio $\xi = 1/\hat{\rho}$. For reference, the values of the model parameters are listed in Table 1. The values of α and \bar{B} are variable and are reported with the results in Section 3.

We performed simulations of a binary fluid using the software package LB3D,⁷⁴ that implements the lattice Boltzmann method described in Section 2. The multicomponent lattice Boltzmann model is solved in a cubic box of size $L_V = 256\Delta x$

Table 1 Summary of the parameters of the numerical model and the values used in the simulations

Parameter	Value
$L_V/\Delta x$	256
$\rho \cdot (\Delta x)^3/\Delta m$	0.7
$\nu \cdot \Delta t/(\Delta x)^2$	1/6
$\sigma \cdot (\Delta t)^2/\Delta m$	0.0267
$\tau/\Delta t$	1
$g \cdot \Delta m(\Delta t)^2/(\Delta x)^5$	0.08
ϕ_f	0.5
ϕ_p	0.15
n_p	1200
$\rho_p \cdot (\Delta x)^3/\Delta m$	1
$V_p/(\Delta x)^3$	$2000\pi/3$
$m/(\Delta i(\Delta x)^2)$	1
$d_c/\Delta x$	2/3
$K_H \cdot (\Delta x)^{1/2}(\Delta t)^2/\Delta m$	100

with periodic boundary conditions. The simulation box is filled with equal volume fractions $\phi_f = 0.5$ of two fluids, initially homogeneously mixed with a density $\rho = 0.7\Delta m/(\Delta x)^3$. The BGK relaxation time is set to $\tau = \Delta t$ and the Shan–Chen interaction strength is set to $g_{kk^*} = 0.08(\Delta x)^2/(\Delta m(\Delta t)^2)$. We performed preliminary simulations of a spherical droplet with these parameters and fitted the pressure difference inside and outside the droplet to the Young–Laplace law, which yielded a surface tension $\sigma = 0.0267\Delta m/(\Delta t)^2$. To study the influence of anisotropic particle shapes on the bijel formation, we performed simulations for particles with three different aspect ratios: $\alpha = 1$ for spherical particles, $\alpha = 2$ for prolate ellipsoids, and $\alpha = 1/2$ for oblate ellipsoids. To match the particle volume fraction ϕ_p between the different particle shapes, we kept the volume of the particles fixed and used the same number of particles for each aspect ratio. The radius along the symmetry axis of the particles was calculated from $V_p = (4/3)\pi R_{\parallel}^3/\alpha^2$, yielding $R_{\parallel} = 7.9\Delta x$ for spheres, $R_{\parallel} = 12.6\Delta x$ for prolate ellipsoids, and $R_{\parallel} = 5\Delta x$ for oblate ellipsoids, respectively. Particles were added to the fluid by placing them randomly inside the box. The lubrication cutoff distance was set to the value $d_c = (2/3)\Delta x$ recommended by Ladd,⁶⁰ and the strength of the Hertz potential was set to $K_H = 100\Delta m/((\Delta x)^{1/2}(\Delta t)^2)$. We first equilibrated the particle positions and orientations by evolving only the equations of motion of the particles, while the fluid remained in its initial configuration, until the minimum particle distance exceeded $1.2 \cdot \max(R_{\parallel}, R_{\parallel}/\alpha)$. After the equilibration, the magnetic flux density $\mathbf{B} = B\hat{\mathbf{z}}$ was switched on and the full system was evolved for 10^5 timesteps. In the course of the simulation, the binary mixture undergoes spinodal decomposition. The particles adsorb at the coarsening interface and eventually become jammed, resulting in the bicontinuous phase morphology of the bijel.

It is worth discussing briefly the possible realization of our model in experiments. A common choice for bijel formation in binary liquids is a mixture of water and lutidine.^{14,15} The surface tension between the phases of a water–lutidine system at 40 °C is around $\sigma = 0.22 \text{ mN m}^{-1}$ and the dynamic viscosity of the lutidine-rich phase is around $\eta = 2.38 \text{ mPa s}$.⁷⁵ Ellipsoidal particles with various aspect ratios can be formed by mechanically stretching spherical particles.⁷⁶ Such particles can be magnetically functionalized by e-beam deposition of a Nickel layer. Fei *et al.*^{77,78} fabricated coated 4 μm polystyrene particles with a permanent magnetic dipole moment of $m \approx 3 \times 10^{-14} \text{ A m}^2$. It was shown that the dipole moment is oriented in the direction parallel to the coated interface,^{72,73} *i.e.*, it can be aligned with the axis of ellipsoidal particles. For the given surface tension, the capillary torque on a particle adsorbed at an interface is approximately $8.8 \times 10^{-16} \text{ N m}$. We thus can estimate that a magnetic flux density of 30 mT is able to exert a magnetic torque that exceeds the capillary torque. We note that under these conditions, the dipole–dipole interaction is on the order of 10^{-16} J and an order of magnitude smaller than the particle–interface interaction which is of order 10^{-15} J . For these bijel properties and the parameters given in Table 1, the spatial resolution of our simulations is $\Delta x \approx 252 \text{ nm}$, and the time step is $\Delta t = 624 \text{ ns}$. This corresponds to a system side length of $L_V \approx 64.5 \text{ } \mu\text{m}$ and a runtime of $T \approx 62.4 \text{ ms}$.



3 Results

Bijels can be used as emulsion templates for porous materials with applications including drug delivery, water desalination, and battery electrodes.^{79–82} The transport properties of porous materials depend on the porosity and tortuosity of the void space and can be linked to the phase-separated morphology of the bijel template. Therefore, we study the domain size and tortuosity of the phase morphology of bijels stabilized by anisotropic particles. In particular, we investigate the effect of magnetic particles on the microstructure of bijels that are formed in external magnetic fields. We simulated bijels with a particle volume fraction of $\phi_p = 0.15$ and varied the magnetic flux density such that the Bond numbers varies in the range $0 \leq \bar{B} \leq 1$. In this work, we use a fixed particle volume fraction and focus on the dependence of the bijel structure on the magnetic field. Bijels with varying particle loading and surface tension and have been studied elsewhere in the literature, *e.g.*, by Hijnen *et al.*⁴⁰ and Jansen and Harting.⁶⁵

Fig. 1 shows snapshots of the bijel microstructure observed at different times with and without an external magnetic field. The figure illustrates how anisotropic particles align with the direction of the magnetic field. As the particles reorient, they can deform the interface which thus responds by rearrangements including reorientation and domain coalescence or breakup. This results in apparently larger domain sizes for bijel formation in magnetic fields. The quantitative effect on the

bijel morphology, and domain size in particular, is analyzed in the following sections.

3.1 Structure factor and domain size of magnetically responsive bijels

In LB simulations of spinodal decomposition,^{83,84} a characteristic length scale can be obtained from the structure factor

$$S(\mathbf{k}, t) = \tilde{\phi}(\mathbf{k}, t)\tilde{\phi}(-\mathbf{k}, t) \quad (27)$$

where $\tilde{\phi}(\mathbf{k}, t)$ is the Fourier transform of the order parameter fluctuations $\phi(\mathbf{x}, t) - \langle \phi \rangle$. A common measure of domain size uses the spherically averaged structure factor

$$S(k, t) = \frac{1}{n_k} \sum_{k-\frac{\Delta}{2} < k < k+\frac{\Delta}{2}} \tilde{\phi}(\mathbf{k}, t)\tilde{\phi}(-\mathbf{k}, t), \quad (28)$$

where $k = |\mathbf{k}|$ denotes the modulus of \mathbf{k} and n_k is the number of lattice sites in a shell of radius k and thickness $\Delta = 2\pi/L_V$. The average domain size can then be defined in terms of the n -th moment of the structure factor⁸⁵

$$L_n(t) = 2\pi \left(\frac{\sum_k S(k, t)}{\sum_k k^n S(k, t)} \right)^{\frac{1}{n}}. \quad (29)$$

It is worth noting that this definition of average domain size does not necessarily yield values that coincide with the typical domain size observed visually in snapshots such as those shown in Fig. 1. However, in a dynamic scaling regime, different measures of domain size are expected to differ only by a constant ratio. We found that the commonly used measure $L_1(t)$ tends to overestimate the observed domain size. Numerically, the calculation of the spherically averaged structure factor is subject to poor statistics in the low k -shells, where the average $|\mathbf{k}|$ of the lattice sites differs from the nominal shell radius. Additionally, the measurement of $L(t)$ in simulations with periodic boundary conditions is subject to finite size effects. More importantly, in suspensions of anisotropic particles, we cannot expect that the structure factor is isotropic. Therefore, we also used the 3D structure factor to calculate a lateral domain size in each Cartesian direction from the second moments^{39,65}

$$L_\beta(t) = 2\pi \sqrt{\frac{\sum_k S(\mathbf{k}, t)}{\sum_k k_\beta^2 S(\mathbf{k}, t)}}. \quad (30)$$

This allows us to compute a domain size parallel ($L_\parallel = L_z$) and perpendicular ($L_\perp = (L_x + L_y)/2$) to the direction of \mathbf{B} separately. The average domain size $L_d(t)$ is computed as $L_d(t) = \sum_\beta L_\beta(t)/3$.

$$L_d(t) = 2\pi \sqrt{\frac{\sum_k S(\mathbf{k}, t)}{\sum_k \sum_\beta k_\beta^2 S(\mathbf{k}, t)}}. \quad (31)$$

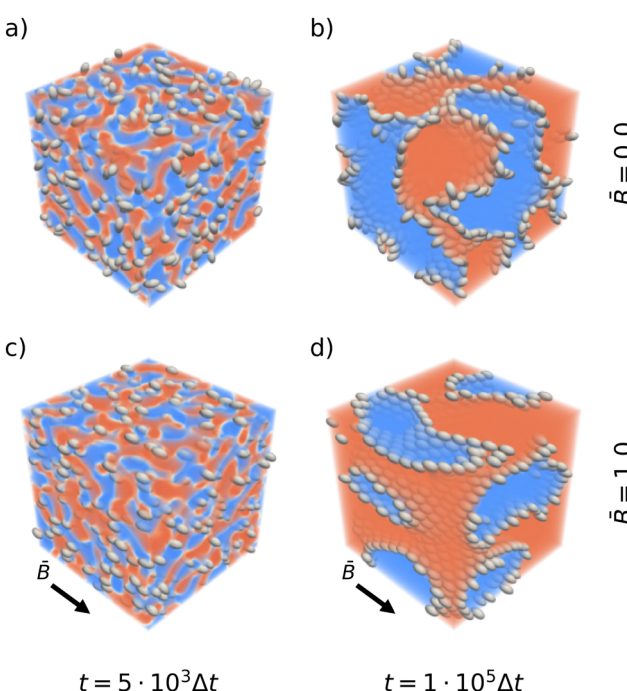


Fig. 1 Snapshots of emulsion gels stabilized by prolate ellipsoids after $t = 5 \times 10^3$ timesteps (left) and after 10^5 timesteps (right). The top row shows the structure forming without a magnetic field. The bottom row shows the structure forming in an applied magnetic field of reduced strength $\bar{B} = 1.0$. The snapshots are colored according to the order parameter ϕ .



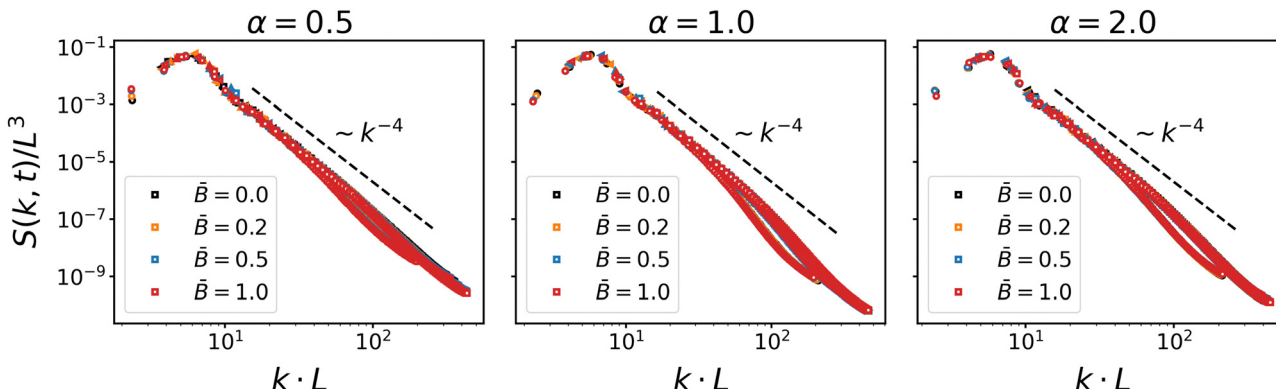


Fig. 2 Scaling plot of the dynamic structure factor $S(k, t)$ for different particle shapes α and at different magnetic field strength \bar{B} . The structure factor is plotted at four different timesteps for each case. The good data collapse shows that the bijel formation is driven by spinodal decomposition. The decay to the right of the peak is reasonably well described by Porod's law $S(k) \sim k^{-4}$.

Before calculating the structure factor $S(\mathbf{k}, t)$, we first filled the lattice sites covered by particles with the average density at the surrounding lattice sites. We employed an iterative procedure that fills the particles layer by layer, starting at the surface layer and using eqn (18) to approximate the density at solid nodes that have at least one neighboring fluid node. This is repeated until all solid nodes have been filled with fluid. The order parameter $\phi(\mathbf{x}, t)$ was then calculated for the filled density fields $\rho_k(\mathbf{x}, t)$. Filling the lattice sites covered by particles is crucial to avoid spurious oscillations of the structure factor at length scales corresponding to the particle size.

Fig. 2 shows the scaling of the dynamic structure factor $S(k, t)$. The data collapse is good, albeit deviations from dynamic scaling are present at smaller length scales. The decay to the right of the maximum is reasonably well described by Porod's law $S(k) \sim k^{-4}$ indicating scattering off a nearly flat interface. These results are in line with the scaling results by Kendon *et al.*^{83,84} for spinodal decomposition of binary fluids, which suggests that the formation of bijels is primarily driven by the separation dynamics of the fluids. The effect of the suspended particles only comes into play once larger domains have formed and the coarsening interface reduces the accessible area to the

point where the particles start interacting. The onset of particle interactions and subsequent jamming leads to a fairly sudden slow-down of domain growth, as can be observed in the time evolution of the domain size shown in Fig. 3.

The domain size L_1 obtained from the spherically averaged structure factor initially shows a power law behavior very close to $L_1 \sim t^{2/3}$. A nonlinear curve fit of the function $b(t - t_0)^\alpha$ to the interval $t \in [0, 3 \times 10^5 \Delta x]$ yields the exponents $\alpha = 0.6448$ for spherical particles, $\alpha = 0.6083$ for oblate particles with aspect ratio $\alpha = 0.5$, and $\alpha = 0.652$ for prolate ellipsoids with aspect ratio $\alpha = 2$. These values are in good agreement with the exponent $\alpha = 2/3$ that is expected in an inertial scaling regime, where the characteristic velocity $U = dL/dt$ scales with the characteristic length scale $U \sim \sqrt{\sigma/(\rho L)}$, leading to $L \sim t^{2/3}$. After around 30 000 to 40 000 time steps, the domain growth starts slowing down and approaches a plateau at $L_1 \approx 200 \Delta x$ for spherical particles, $L_1 \approx 180 \Delta x$ for the prolate particles, and $L_1 \approx 170 \Delta x$ for the oblate particles. Interestingly, the alternative domain size measure L_d obtained from the second moments of the 3D structure factor does not show the same power law behavior. The rate of increase of L_d is substantially smaller than that of L_1 , with a fitted exponent in the range of

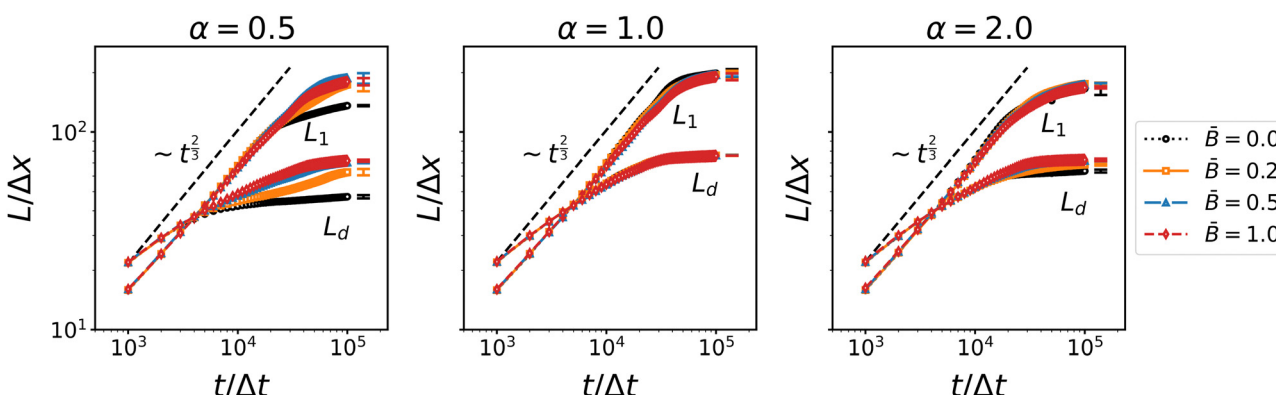


Fig. 3 Time dependence of the average domain size of the bijel for different particle shapes α and at different magnetic field strength \bar{B} . L_1 denotes the domain size obtained from the first moment of the spherical average structure factor, and L_d denotes the domain size obtained from the second moment of the 3D structure factor. The increase roughly follows a $\sim t^{2/3}$ scaling law indicative of the inertial regime of spinodal decomposition.



0.12 to 0.20. The increase of L_d levels off earlier and reaches a plateau around $L_d \approx 70\Delta x$ for all three particle aspect ratios. While dynamic scaling allows different measures of the characteristic length scale to vary by a prefactor, the deviation from the expected power law of both viscous and inertial scaling indicates that the second moment of the 3D structure factor does not yield a proper characteristic length scale. If one interprets the moments of the structure factor as moments of a probability distribution, then the second moment of the 3D structure factor is equivalent to the ratio of the fourth and second moments of the spherically averaged structure factor (due to the factor k^2 in the volume integral). Hence L_d is perhaps better interpreted as describing the shape of the structure factor (similar to kurtosis, but not exactly the same) rather than a characteristic length scale. Nevertheless, the second moments L_β provide separate measures for the three Cartesian directions and can thus reveal anisotropy of the domain morphology.

3.2 Effect of magnetic field on bijel formation

At first glance, the time-dependence of the domain size in Fig. 3 suggests that the domain size is not strongly affected by the external magnetic field. In Fig. 4, we plotted the domain size measure L_d normalized by R , the larger of the two radii of the ellipsoidal particles. The data points represent the domain size measured at the final time step and averaged over three independent simulation runs with the same parameters. The normalization with the particle radius makes it apparent that the ellipsoidal particles reduce the domain size of bijels. This observation is in line with observations by Günther *et al.*³⁹ and indicates that – relative to their volume – ellipsoidal particles stabilize a larger interface area than spherical particles. This is due to the larger cross-sectional area of ellipsoidal particles at the same volume. Furthermore, steric constraints prevent anisotropic particles to pack less densely in the interface than spherical particles, as we will discuss in more detail below.

The magnetic field does have an effect on the directional domain size as shown in Fig. 4 where we plotted the domain size in the direction parallel and perpendicular to \mathbf{B} separately. We find that for prolate particles, the domain size in the parallel

direction increases with the field strength up to approximately three particle radii for the largest field, while the perpendicular domain size stays constant. This trend is reversed for oblate particles for which the domain size in the parallel direction decreases slightly with field strength while the perpendicular domain size increases by approximately four particle radii. Without a field, prolate particles lead to smaller domain size than both spherical and oblate particles, whereas they increase the domain size when the bijel forms under the influence of a magnetic field. The anisotropy is due to the alignment of ellipsoidal particles which leads to a closer packing within the interface akin to nematic ordering. The difference between oblate and prolate particles is caused by the orientation of the magnetic dipole moment \mathbf{m} along the symmetry axis of the particles. In our model, \mathbf{m} is aligned with the larger axis of prolate ellipsoids, whereas it is aligned with the smaller axis of oblate ellipsoids. Hence \mathbf{m} lies in the plane of the larger cross-section of prolate particles while \mathbf{m} is perpendicular to the larger cross-section of oblate particles. We thus expect that alignment of the particles with the magnetic field \mathbf{B} facilitates closer packing perpendicular to the field for prolate particles, and parallel to the field for oblate particles. The increase/decrease of domain size levels off at intermediate field strength and further increases of the field have no additional effect.

3.3 Tortuosity

The anisotropy of domain size suggests that the magnetic field influences the bijel morphology at the microscale. To investigate whether these structural changes have an effect on macroscopic transport properties, we also characterized the tortuosity of the bijels. Various definitions of tortuosity have been proposed in the literature,⁸⁶ including geometric, diffusional, and hydraulic tortuosity. Here we use the diffusional tortuosity $\tau = \varepsilon D/D_{\text{eff}}$, *i.e.*, the ratio of the effective diffusivity D_{eff} and the intrinsic diffusivity D . Porous structures were generated from the order parameter field at the last time step of the simulations by binarizing the raw order parameter data using a threshold of zero. We masked the largest connected component representing the percolating domain and then used the Python package taufactor⁸⁷ to calculate the tortuosity in the three Cartesian coordinate directions. Taufactor determines the tortuosity by comparison of steady-state diffusive flow through a porous medium with the bulk diffusive flow in a control volume of the same size, molecular diffusivity, and driving force.⁸⁷ We used the PeriodicSolver to employ periodic boundary conditions.

Fig. 5 shows the results for the tortuosity as a function of the applied magnetic flux for the three particle aspect ratios. In the absence of a magnetic field, the three aspect ratios lead to a similar tortuosity around $\tau \approx 1.5$, slightly larger than the tortuosity predicted by the Bruggeman relation $\tau = \varepsilon^{-0.5} = 1.41$ for equal volume fractions $\varepsilon = 0.5$ of the phases.^{88,89} The observed tortuosity is consistent with simulations of gyroid structures by Luo *et al.*, who found diffusive tortuosities in the range from 1.48 to 1.73.⁹⁰ Fig. 5 shows that in an applied magnetic field, the tortuosity of bijels stabilized by anisotropic particles ($\alpha \neq 1$) becomes anisotropic as well. Oblate particles ($\alpha = 0.5$) lead to an increase of the tortuosity τ_{\parallel} in the direction

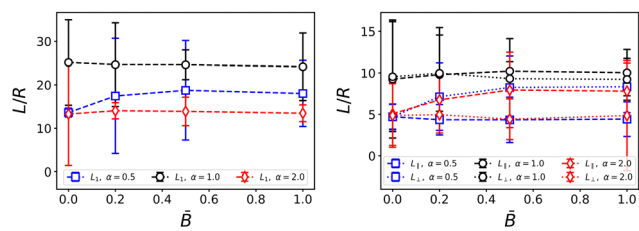


Fig. 4 Dependence of the average domain size on the magnetic field strength \tilde{B} . The left plot shows the average domain size L_1 obtained from the spherically averaged structure factor. The right plot shows the parallel and perpendicular domain size obtained from the respective second moments of the 3D structure factor. Errorbars indicate the standard deviation taken over three independent simulation runs. For anisotropic particles, the directional domain size becomes more anisotropic with increasing field strength.



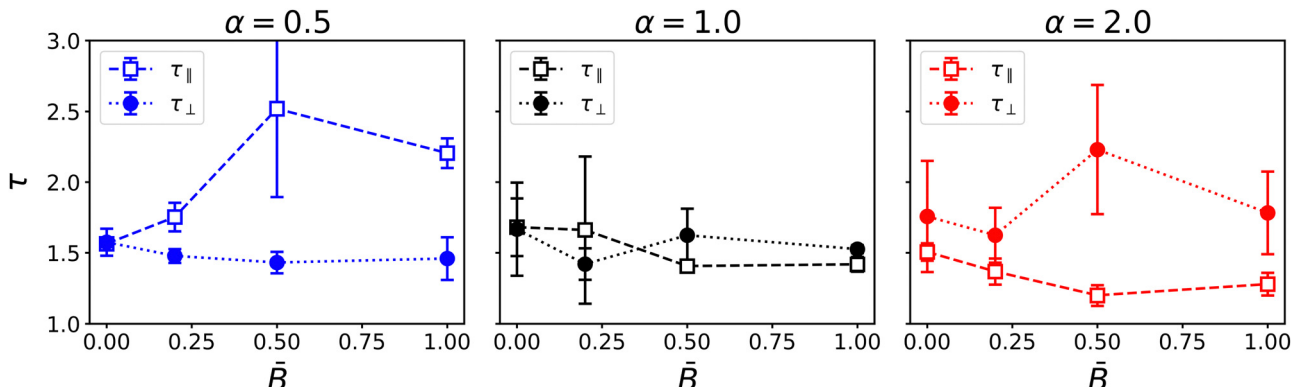


Fig. 5 Dependence of the tortuosity on the magnetic field strength \bar{B} for different particle shapes α . Different components of the tortuosity tensor show the anisotropy for oblate and prolate particles.

of the magnetic field while the tortuosity in the direction perpendicular to the magnetic field remains around $\tau_{\parallel} \approx 1.5$. Conversely, prolate particles ($\alpha = 2$) lead to an increase of the tortuosity in the direction perpendicular to the magnetic field, while the tortuosity in the parallel direction slightly decreases with increasing field strength. In both cases, the changes in tortuosity are consistent with the anisotropic domain size and the alignment of particles with the magnetic field. For prolate particles, the longer axis is aligned with the magnetic moment and induces larger domain size and lower tortuosity in this direction. The results show that the magnetic field has a noticeable effect on the tortuosity of the bijel. We observe that the largest change of tortuosity is measured at intermediate field strength $\bar{B} = 0.5$. This suggests that the competition of interfacial and magnetic forces and the resulting alignment of particles and liquid domains induces morphological changes that are more complex than a monotonic increase or decrease. We therefore turn to investigate the microstructural changes within the bijel morphology in more detail.

3.4 Kinetics of bijel formation in magnetic fields

To shed light on the mechanisms involved in the coarsening dynamics, we now turn to the kinetics of bijel formation in more detail. The coarsening dynamics can be characterized by a

coarsening speed. Here, we use the finite difference of the directional domain size to calculate the components of the coarsening velocity

$$u_{L_{\beta}}(t) = \frac{L_{\beta}(t + \Delta t_s) - L_{\beta}(t - \Delta t_s)}{2\Delta t_s}, \quad (32)$$

where Δt_s is the time between simulation snapshots, and β denotes either the direction parallel or perpendicular to the magnetic field.

Fig. 6 shows the coarsening speed in the directions parallel and perpendicular to the applied magnetic field. The data confirms that for spherical particles, domain coarsening remains isotropic. We observe a higher coarsening speed initially which slows at later times when the particles begin to jam. This indicates that the coarsening is subject to different time scales, as reported previously by Harting and co-workers.³⁹ Reeves *et al.*⁹¹ have pointed out that bijel formation hinges on the jamming time in relation to the disruption time, *i.e.*, the time scale at which domain pinch-off events can cause bijel break-up through depercolation. In our simulations, however, we have not observed disruption of bijel formation; stable bijels form for all parameters consistent with simulations by Stratford *et al.*¹³ and Jansen *et al.*⁶⁵

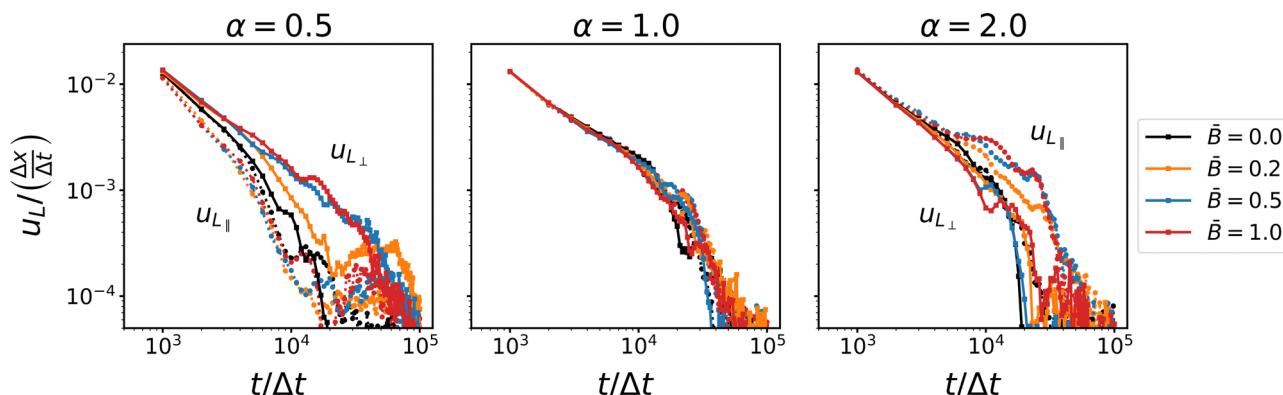


Fig. 6 Time-dependence of the coarsening velocity u_L for different particle shapes α and at different magnetic field strength \bar{B} . The different components of the coarsening velocity show that the jamming time is different in the direction parallel and perpendicular to the magnetic field.



For ellipsoidal particles, our data clearly shows that anisotropic domain coarsening arises in magnetic fields. For oblate particles ($\alpha = 0.5$), the coarsening speed in the direction perpendicular to the field increases with increasing magnetic field strength. Jamming in this direction appears to be delayed compared with the direction parallel to the field. The coarsening speed in the parallel direction remains comparable to the case without an applied magnetic field. This anisotropic behavior of the coarsening speed reverses for prolate particles, where the coarsening speed in the direction parallel to the field increases with increasing field strength, and jamming in this direction is delayed compared with the perpendicular direction. In addition, we observe a shoulder (around $10^4\Delta t$) where the coarsening speed decays more slowly before jamming sets in. These results suggest that the coarsening near the jamming time is affected by a mechanism that depends on the applied magnetic field and causes the anisotropic behavior. This mechanism involves the re-orientation of anisotropic particles and their alignment relative to the direction of the magnetic field. To confirm this hypothesis, we analyze the orientational order of the particles and their alignment relative to the magnetic field and the interface, respectively.

3.5 Particle re-orientation and packing

The primary effect of the magnetic field is the torque it exerts on the magnetic dipole of the particles. This torque rotates the particles towards the direction of the magnetic field. The alignment of the particles with the field direction can be clearly observed in the simulation snapshots shown in Fig. 7. While the particles are oriented randomly in the interface in the absence of a magnetic field ($\bar{B} = 0$), the magnetic field induces orientational order of the magnetic dipoles (shown for $\bar{B} = 1$). To measure the particle alignment quantitatively, we computed the nematic order tensor⁹²

$$Q = \frac{1}{n_p} \sum_i \left(\frac{3}{2} \hat{\mathbf{o}}_i \otimes \hat{\mathbf{o}}_i - \frac{1}{2} \mathbf{I} \right), \quad (33)$$

where $\hat{\mathbf{o}}_i$ is the orientation of the i -th particles and n_p is the number of particles in the system. The largest eigenvalue of Q yields the nematic order parameter

$$S = \left\langle \frac{3}{2} \cos^2(\theta) - \frac{1}{2} \right\rangle, \quad (34)$$

where $\theta = \arccos(\hat{\mathbf{o}}_i \cdot \hat{\mathbf{n}})$ is the angle between the particle orientation and the nematic director $\hat{\mathbf{n}}$.

Fig. 8 shows the time evolution of the nematic order parameter S for the three different particle aspect ratios α and varying magnetic field strength \bar{B} . The onset of orientational order is nearly instantaneous and increases with increasing field strength. For magnetic flux densities $\bar{B} \geq 0.5$, the nematic order parameter saturates at $S \approx 1.0$ towards the end of the simulation. For the prolate particles ($\alpha = 2.0$), we observe a shoulder at around $10^4\Delta t$ and an intermittent plateau. The occurrence of this plateau coincides with the slowed decay of the coarsening speed in Fig. 6. This change in the orientational ordering is even more distinct for the oblate particles, where

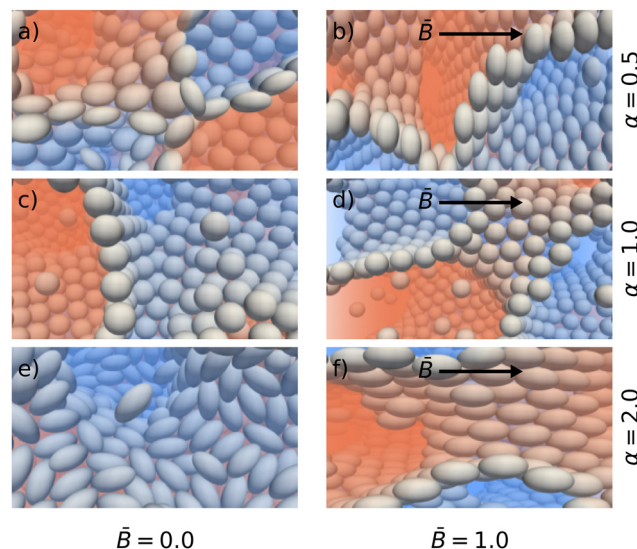


Fig. 7 Snapshots illustrating the particle packing at the interface for different particle shapes α with (left) and without (right) applied magnetic field \bar{B} . The right column shows the alignment of the symmetry axis of the oblate (top row) and prolate (bottom row) particles in the direction of the magnetic field indicated by arrows.

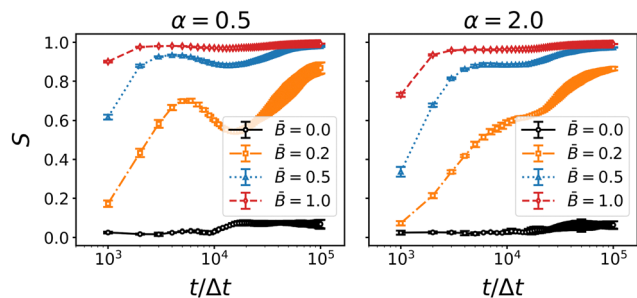


Fig. 8 Time-dependence of the nematic order parameter S of oblate ($\alpha = 0.5$) and prolate ($\alpha = 2.0$) particles at different field strength \bar{B} . Errorbars indicate the standard deviation taken over three independent simulation runs. Nematic order generally increases with applied field strength for all particle geometries. The increase slows down (for prolate particles) or reverses (for oblate particles) around 10^4 timesteps.

the nematic order decays intermittently before it increases again. The intermittent decay for oblate particles, and the plateau for prolate particles, correlate with the delayed onset of jamming in the direction perpendicular and parallel to the magnetic field, respectively. These observations can be interpreted as follows: the magnetic field aligns the particles with the direction of the magnetic field early during the simulation. Due to this alignment, the steric constraints between particles adsorbed at the interface are reduced which allows further coarsening of the interfacial area. However, during coarsening, the interfaces may re-orient themselves and cause a capillary torque on the particles that competes with the magnetic torque. This competition intermittently perturbs the nematic order of the particles leading to the observed decay and plateau of the nematic order parameter. Accordingly, the decay of S is most pronounced at the weakest magnetic field $\bar{B} = 0.2$.



To further corroborate this mechanism, we quantify the orientational order of the interfaces. We computed the interfacial orientation tensor

$$Q_{\text{int}} = \frac{1}{\langle \text{tr}(\mathbf{A}) \rangle} \left\langle \mathbf{A} - \frac{1}{3} \text{tr}(\mathbf{A}) \mathbf{1} \right\rangle, \quad (35)$$

where the local tensor field \mathbf{A} is defined by

$$\mathbf{A} = \nabla \phi \otimes \nabla \phi. \quad (36)$$

The largest eigenvalue of Q is taken as the interface nematic order parameter S_{int} .

The results for the interface nematic order parameter S_{int} are shown in Fig. 9. The nematic interface alignment increases over time and the rate of increase appears to be higher for larger magnetic field strength \bar{B} . In all cases, the final value of S_{int} is below 0.5 indicating that the tortuous structure of the interface is maintained in the presence of magnetic fields. This confirms that the re-orientation of the particles does not disrupt the bijel structure but leads to partial alignment of the interfaces without changing the general topology of the bicontinuous morphology.

When the particles rotate, the interface exerts a capillary torque on the particles due to the surface tension and the contact angle. If the magnetic torque exceeds the interfacial forces, the particles can potentially overcome the capillary torque and rotate out of the interface. For prolate particles ($\alpha = 2$) adsorbed at flat interfaces, Davies *et al.* have shown that a transition between the energetically preferred “flat” orientation and a tilted orientation occurs at a critical field strength of approximately $\bar{B} = 0.2$.^{36,46,93} In the case of bijels, however, the percolating interfaces are tortuous and thus more mobile. We therefore posit that, rather than tilting out of the interface, rotating particles can “pull” the interface along and thereby align the liquid domains. For anisotropic particles, we expect that the interfaces align along the larger cross-section of the particles, *i.e.*, perpendicular to the symmetry axis of oblate particles and parallel to the symmetry axis of prolate particles. The data for the anisotropic domain size and tortuosity above is consistent with this assumption. To ascertain that the particles

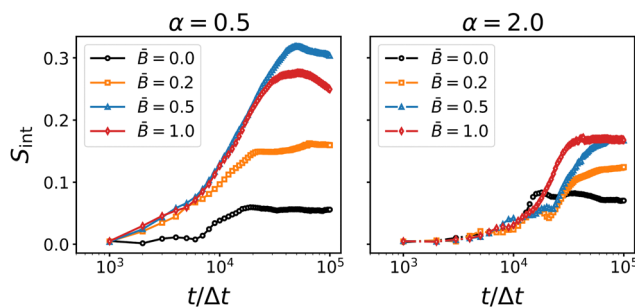


Fig. 9 Time-dependence of the interface nematic order for oblate ($\alpha = 0.5$) and prolate ($\alpha = 2$) particles at different magnetic field strength \bar{B} . The interface alignment tends to increase with increasing field strength. The rate of increase becomes larger around 10^4 timesteps, indicating the alignment of the interfaces due to capillary interactions with the particles.

remain indeed in their energetically preferred orientation with respect to the interface, we analyzed the angle between the symmetry axis of the particles and the interface normal. To this end, we generated a mesh of the interface using a marching cubes algorithm. For each particle we identified the mesh vertex closest to the particle’s position (excluding particles whose distance to the mesh exceeds the radius of the longer particle axis) and computed the angle between the particle orientation vector $\hat{\mathbf{o}}_i$ and the interface normal at the closest vertex. Fig. 10 shows the time-dependence of the average angle ψ between the particle dipole axis and the nearest interface normal.

For both types of anisotropic particles, the average angle between the particle dipole and the interface normal is initially around $\psi \approx 60^\circ$. As the spinodal interface sweeps through the system, particles attach to the interface and alignment due to the capillary torque sets in. For oblate particles, the dipole axis aligns with the interface normal as indicated by the decay of ψ towards zero. For prolate particles, the preferential alignment of the dipole axis is parallel to the interface and hence ψ increases towards 90° . The main variation of ψ occur in a time interval around $10^4 \Delta t$ which coincides with the distinct features of the coarsening speed and the particle nematic order observed above. The results thus substantiate the proposed mechanism of particle re-orientation in the magnetic field and the concomitant local alignment of the interface. Once the particles start jamming, the shrinking interfacial area forces some particles out of their preferred alignment with the interface, leading to an increase of ψ for oblate particles and a decrease of ψ for prolate particles. Fig. 10 suggests that the forced tilting is more pronounced for oblate particles than for prolate particles. Due to the larger aspect ratio, the tilting of prolate particles relative to the interface induces deformations that appear to cause a larger capillary torque than the tilting of oblate particles. Hence the prolate particles remain mostly aligned with the interface even in the stronger applied magnetic fields.

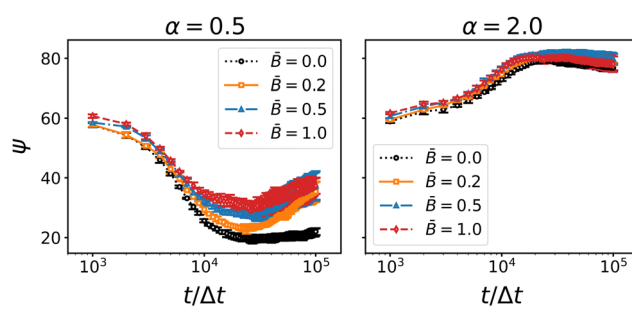


Fig. 10 Time-dependence of the average angle ψ between the particle axis and the interface normal for oblate ($\alpha = 0.5$) and prolate ($\alpha = 2$) particles at different magnetic field strength \bar{B} . Errorbars indicate the standard deviation taken over three independent simulation runs. The angle between between the particles and the interface normal generally approaches the energetically preferred value (0° for oblate particles, 90° for prolate particles). The average angle changes most rapidly around 10^4 timesteps.



As hypothesized above, the alignment of the particle dipole axis with the magnetic field reduces the steric constraints within the interface. To corroborate this idea, we analyzed the radial distribution function (RDF) of the particles

$$g(r) = \frac{n_p - 1}{n_p} V \langle \delta(r - r_i) \rangle, \quad (37)$$

where n_p is the number of particles in the volume V , and $\langle \cdot \rangle$ denotes an average over all particles. The radial distribution

function was calculated by binning the distance between all particle pairs and normalizing the shells with respect to the distribution $4\pi r^2 dr$ of an ideal gas. The time-evolution of the RDFs for the three particle shapes and varying magnetic flux density is illustrated in Fig. 11.

The radial distribution function is shown at time steps $t = 1000\Delta t$, $10000\Delta t$, $100000\Delta t$. For ellipsoidal particles, the characteristic distances between particles in contact are $2R_{\parallel}$, $2R_{\perp}$, and $R_{\parallel} + R_{\perp}$. These distances are marked by dashed lines in

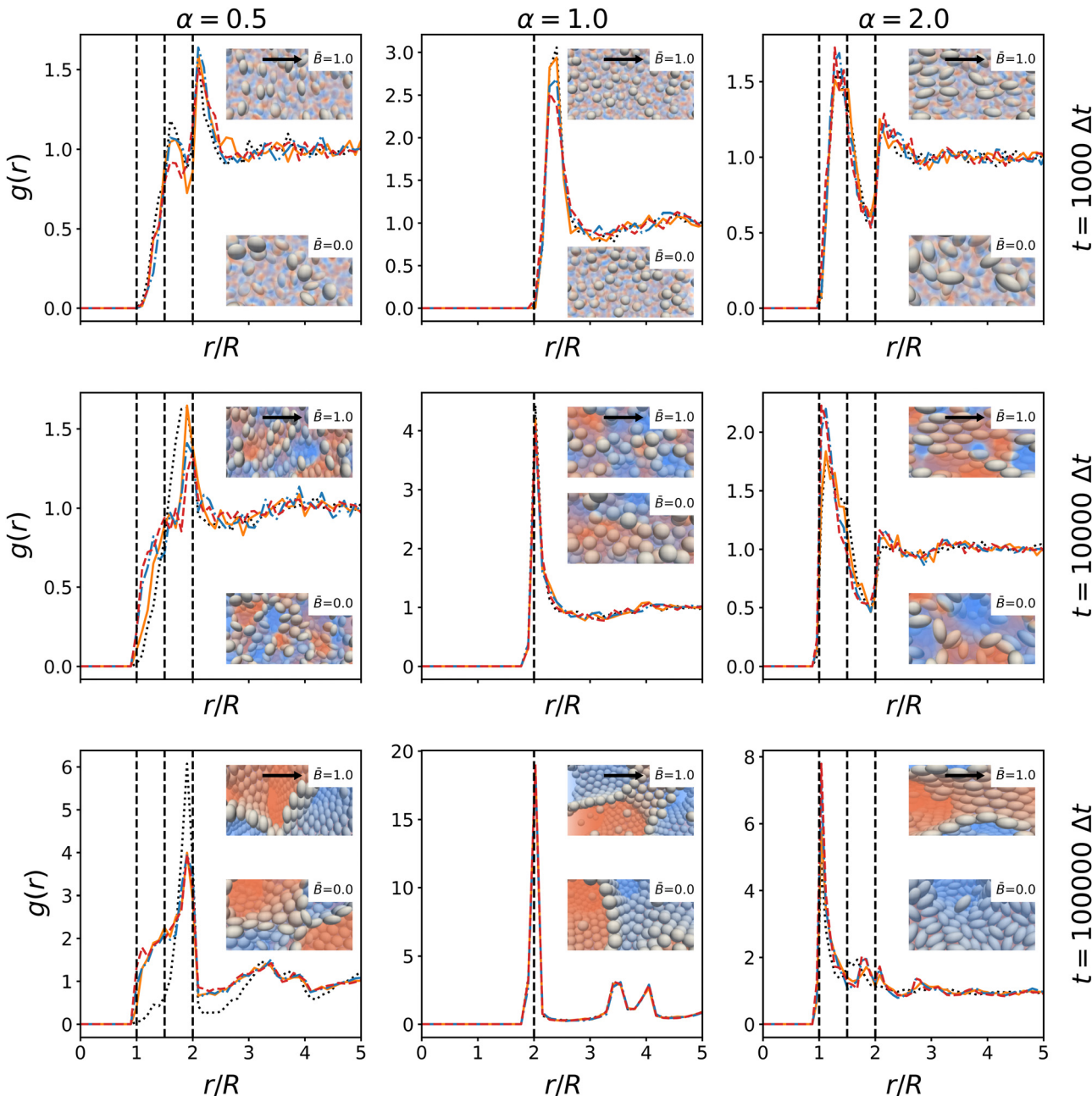


Fig. 11 Time-evolution of the radial distribution function $g(r)$ of the particles at different magnetic field strength \tilde{B} . The radial distribution function is shown at 10^3 , 10^4 , and 10^5 timesteps. The distance r is normalized by the radius $R = \max(R_{\parallel}, R_{\perp})$ of the larger particle axis. The peaks illustrate the packing of particles in the interface. Dashed lines indicate the side-by-side, tip-to-tip, and side-to-side configuration of particle pairs. For spherical particles, the three values are identical. The insets show snapshots of the particle arrangement with and without magnetic field at the respective timesteps. The direction of the magnetic field is indicated by arrows.

Fig. 11. We observe that the largest peak of the RDF coincides with the distance $2R_{\perp}$ for both oblate and spherical particles, indicating that oblate particles tend to be in contact at their circumference while prolate particles preferentially align side-by-side. These arrangements lead to closer packing of particles in the interface. The peaks are less pronounced in the early stage of the simulations, where the particles are more randomly oriented. Notably, there is a dip in the RDF of prolate particles at $2R_{\parallel}$ indicating that initially the tip-to-tip configuration occurs more rarely. The growth of the peak height over time shows that the magnetic fields promote this alignment compared to the case without magnetic field. For oblate particles, a shoulder develops around $R_{\parallel} + R_{\perp}$, indicating that some particles tilt out of the interface to reduce the covered interfacial area. For prolate particles, the dip at $2R_{\parallel}$ disappears over time, indicating that more particles align tip-to-tip. This is consistent with alignment of prolate particles with respect to the magnetic field, which facilitates closer packing along both axes of the particles. It further suggests that particles arrange in layers, which can also be observed in the snapshot in Fig. 7. Together with the analysis of nematic order above, these results substantiate the proposed mechanisms that influence the formation of bijels with anisotropic particles in magnetic fields: the magnetic field aligns the particle dipole axis in the field direction, and the particle re-orientation couples to interface alignment due to the capillary interactions. The alignment of particles reduces the steric constraints within the interface, which allows the interface to shrink further and facilitates domain coarsening. In terms of the time-evolution, the rotation of particles due to the magnetic field occurs during the initial stages of the simulation, followed by the local re-alignment of interfaces due to capillary interactions. In the case of prolate particles, we observed the shrinking interface can force particles to tilt out of their preferential alignment to facilitate closer packing. Generally, our results show that when bijels stabilized by anisotropic magnetic particles form under the influence of a magnetic field, the domain size and tortuosity become anisotropic. Additionally, we observe that the particle packing in the interface becomes more ordered due to the alignment effects.

4 Conclusions

In this work, we studied the effect of applied magnetic fields on the formation of bijels stabilized by magnetic ellipsoidal particles. We considered oblate, spherical, and prolate particles with a permanent magnetic dipole moment suspended in a symmetric binary liquid. We found that, while the overall formation of a bijel is not disrupted by magnetic interactions, bijels stabilized by oblate or prolate ellipsoids exhibit anisotropic domain size and an anisotropic tortuosity. For oblate particles, the domain size increases in the direction perpendicular to the magnetic field while the tortuosity increases in the parallel direction. Conversely, for prolate particles, the domain size increases in the direction parallel to the magnetic field while the tortuosity increases in the perpendicular direction.

Compared with bijels formed in the absence of a magnetic field, we observed changes in domain size up to 30% for non-spherical particles. This effect can be explained by the re-orientation of the particle dipole axis with the magnetic field, which in turn re-aligns the interfaces in the direction of the longer axis of the particles. We further corroborated this mechanisms by analyzing the coarsening speed and the nematic order of the particles and the interfaces. We found that jamming of particles is delayed in the direction of the longer ellipsoidal axis leading to enhanced coarsening in this direction. The timescale of the delayed jamming coincides with a slow-down of the orientational ordering of the particles whereas the alignment of the interfaces increases. We also found that the angle between the particle dipole axis and the interface normal changes at this stage. Additionally, we analyzed the radial distribution function of the particles and found that prolate particles tend to align side by side, while the oblate particles exhibit a less regular arrangement. Based on these findings, we propose that bijel formation in magnetic fields is governed by two coupled effects: during the initial stage, the magnetic torque rotates the particles to align the magnetic dipole moment with the field, and the orientational order of the particles facilitates further coarsening. As coarsening proceeds, the capillary interactions cause the interfaces to align with the longer particle axis. The shrinking interface compresses the particles into ordered arrangements. When jamming sets in, some particles can be forced to tilt out of the interface and this effect is more prominent for oblate particles.

Our results demonstrate the effects of magnetic fields on the structural properties of bijels stabilized by ellipsoidal magnetic particles. This control is desirable in applications where the domain size and tortuosity affect the transport properties. For example, reduced tortuosity can increase the diffusive permeability of bone-like materials.⁹⁴ Similarly, low tortuosity in lithium electrodes facilitates homogeneous ion transport and uniform lithium deposition, leading to enhanced cyclability of batteries.^{95,96} Whereas we have considered one particular regime of spinodal decomposition, the viscosity and surface tension of the liquids offer additional parameters that could be leveraged to tune the bijel formation. Moreover, the particle volume fraction is another parameter that is known to affect the formation of particle-stabilized emulsions.^{40,65} With respect to possible experimental realizations of our simulations, we should emphasize that we have generally considered micron-size particles and have neglected thermal fluctuations. At the nanoscale, thermal fluctuations may in principle play a role, however, Reeves *et al.*⁹¹ have shown that nanoparticles benefit from smaller driving forces towards disruptive curvature and actually lead to more robust bijel formation. Nevertheless, the stability of magnetically-responsive bijels is a relevant question for applications that involve shear flows such as crossflow reactors.⁹⁷ Aside from particle-size and shape effects, direct interactions between particles are a possible avenue to tune the formation of particle-stabilized emulsions gels, as the recent discovery of bicontinuous intraphase jammed emulsion gels (bipjels) illustrates.⁹⁸ Another interesting observation arising



from our simulations is that the packing order of particles in the interface appears to increase when bijels form under the influence of a magnetic field. While such interfacial ordering effects have been studied on planar interfaces,^{99–101} they have hitherto not been reported for particle-stabilized emulsion gels. It would be interesting to examine the implications of this ordering on the optical and transport properties of jammed emulsion gels. In conclusion, our simulations provide relevant insights into the formation of magnetic particle-stabilized bijels in the presence of external magnetic fields, and they demonstrate the potential of magnetic particles for fabrication of emulsion systems with tunable and anisotropic particle packing and domain structure.

Author contributions

NK: investigation, data curation, visualization, validation, writing – original draft. UDS: conceptualization, methodology, software, investigation, data curation, formal analysis, visualization, funding acquisition, project administration, supervision, writing – original draft, writing – review & editing.

Data availability

The data and code used to generate the figures in this manuscript are available as an interactive notebook on Code Ocean at <https://doi.org/10.24433/CO.6321940.v1>. Due to size limitations, the raw simulation data are available for download on request from the authors.

Conflicts of interest

There are no conflicts to declare.

Acknowledgements

This work was supported by the National Science Foundation under NSF Awards DMR-1944942, DMR-2414458, and OIA-2346036. Any opinions, findings and conclusions or recommendations expressed in this material are those of the authors and do not necessarily reflect those of the National Science Foundation. This work used NCSA Delta at the National Center for Supercomputing Applications through allocation PHY220131 from the Advanced Cyberinfrastructure Coordination Ecosystem: Services & Support (ACCESS) program, which is supported by National Science Foundation grants #2138259, #2138286, #2138307, #2137603, and #2138296. We wish to thank Jens Harting and Alexander Wagner for insightful discussions.

References

- 1 T. Zhang, R. A. Sanguramath, S. Israel and M. S. Silverstein, *Macromolecules*, 2019, **52**, 5445–5479.
- 2 C. Stubenrauch, A. Menner, A. Bismarck and W. Drenckhan, *Angew. Chem., Int. Ed.*, 2018, **57**, 10024–10032.
- 3 B. H. Jones and T. P. Lodge, *J. Am. Chem. Soc.*, 2009, **131**, 1676–1677.
- 4 B. P. Binks, *Adv. Mater.*, 2002, **14**, 1824–1827.
- 5 Z. Abbasian Chaleshtari, M. Zhou and R. Foudazi, *J. Appl. Phys.*, 2022, **131**, 150902.
- 6 B. Aldemir Dikici and F. Claeysens, *Front. Bioeng. Biotechnol.*, 2020, **8**, 875.
- 7 M. A. Mudassir, H. Z. Aslam, T. M. Ansari, H. Zhang and I. Hussain, *Adv. Sci.*, 2021, **8**, 2102540.
- 8 W. Ramsden, *Proc. R. Soc. London*, 1903, **72**, 156–164.
- 9 S. U. Pickering, *J. Chem. Soc., Dalton Trans.*, 1907, **91**, 2001–2021.
- 10 R. Zheng and B. P. Binks, *Langmuir*, 2022, **38**, 1079–1089.
- 11 A. Menner, R. Verdejo, M. Shaffer and A. Bismarck, *Langmuir*, 2007, **23**, 2398–2403.
- 12 M. E. Cates and P. S. Clegg, *Soft Matter*, 2008, **4**, 2132–2138.
- 13 K. Stratford, R. Adhikari, I. Pagonabarraga, J.-C. Desplat and M. E. Cates, *Science*, 2005, **309**, 2198–2201.
- 14 P. S. Clegg, E. M. Herzig, A. B. Schofield, S. U. Egelhaaf, T. S. Horozov, B. P. Binks, M. E. Cates and W. C. K. Poon, *Langmuir*, 2007, **23**, 5984–5994.
- 15 E. M. Herzig, K. A. White, A. B. Schofield, W. C. K. Poon and P. S. Clegg, *Nat. Mater.*, 2007, **6**, 966–971.
- 16 J. W. Tavacoli, J. H. J. Thijssen, A. B. Schofield and P. S. Clegg, *Adv. Funct. Mater.*, 2011, **21**, 2020–2027.
- 17 M. N. Lee, J. H. J. Thijssen, J. A. Witt, P. S. Clegg and A. Mohraz, *Adv. Funct. Mater.*, 2012, **23**, 417–423.
- 18 J. W. Tavacoli, J. H. J. Thijssen and P. S. Clegg, *Particle-Stabilized Emulsions and Colloids: Formation and Applications*, The Royal Society of Chemistry, 2014, pp. 129–168.
- 19 M. F. Haase, K. J. Stebe and D. Lee, *Adv. Mater.*, 2015, **27**, 7065–7071.
- 20 Y. Yabuno, K. Mihara, N. Miyagawa, K. Komatsu, K. Nakagawa, T. Shintani, H. Matsuyama and T. Yoshioka, *J. Membr. Sci.*, 2020, **612**, 118468.
- 21 R. Pang, K. K. Chen, Y. Han and W. S. W. Ho, *J. Membr. Sci.*, 2020, **612**, 118443.
- 22 J. A. Witt, D. R. Mumm and A. Mohraz, *J. Mater. Chem. A*, 2016, **4**, 1000–1007.
- 23 J. S. Samdani, T.-H. Kang, C. Zhang and J.-S. Yu, *ACS Omega*, 2017, **2**, 7672–7681.
- 24 T. J. Thorson, E. L. Botvinick and A. Mohraz, *ACS Biomater. Sci. Eng.*, 2018, **4**, 587–594.
- 25 T. J. Thorson, R. E. Gurlin, E. L. Botvinick and A. Mohraz, *Acta Biomater.*, 2019, **94**, 173–182.
- 26 J. C. Loudet, A. M. Alsayed, J. Zhang and A. G. Yodh, *Phys. Rev. Lett.*, 2005, **94**, 018301.
- 27 J. C. Loudet and B. Pouliquen, *EPL*, 2009, **85**, 28003.
- 28 B. Madivala, S. Vandebril, J. Fransaer and J. Vermant, *Soft Matter*, 2009, **5**, 1717.
- 29 B. Madivala, J. Fransaer and J. Vermant, *Langmuir*, 2009, **25**, 2718–2728.
- 30 N. Bowden, A. Terfort, J. Carbeck and G. M. Whitesides, *Science*, 1997, **276**, 233–235.



31 E. P. Lewandowski, M. Cavallaro, L. Botto, J. C. Bernate, V. Garbin and K. J. Stebe, *Langmuir*, 2010, **26**, 15142–15154.

32 K. J. Stebe, E. Lewandowski and M. Ghosh, *Science*, 2009, **325**, 159–160.

33 L. Botto, L. Yao, R. L. Leheny and K. J. Stebe, *Soft Matter*, 2012, **8**, 4971–4979.

34 M. Cavallaro, L. Botto, E. P. Lewandowski, M. Wang and K. J. Stebe, *Proc. Natl. Acad. Sci. U. S. A.*, 2011, **108**, 20923–20928.

35 E. M. Furst, *Proc. Natl. Acad. Sci. U. S. A.*, 2011, **108**, 20853–20854.

36 F. Bresme and J. Faraudo, *J. Phys.: Condens. Matter*, 2007, **19**, 375110.

37 F. Bresme, *Eur. Phys. J. B*, 2008, **64**, 487–491.

38 F. Günther, F. Janoschek, S. Frijters and J. Harting, *Comput. Fluids*, 2013, **80**, 184–189.

39 F. Günther, S. Frijters and J. Harting, *Soft Matter*, 2014, **10**, 4977–4989.

40 N. Hijnen, D. Cai and P. S. Clegg, *Soft Matter*, 2015, **11**, 4351–4355.

41 S. Melle, M. Lask and G. G. Fuller, *Langmuir*, 2005, **21**, 2158–2162.

42 J. Zhou, X. Qiao, B. P. Binks, K. Sun, M. Bai, Y. Li and Y. Liu, *Langmuir*, 2011, **27**, 3308–3316.

43 U. Dassanayake, S. Fraden and A. van Blaaderen, *J. Chem. Phys.*, 2000, **112**, 3851–3858.

44 M. E. Leunissen, H. R. Vutukuri and A. V. Blaaderen, *Adv. Mater.*, 2009, **21**, 3116–3120.

45 A. R. Morgan, N. Ballard, L. A. Rochford, G. Nurumbetov, T. S. Skelhon and S. A. F. Bon, *Soft Matter*, 2012, **9**, 487–491.

46 G. B. Davies, T. Krüger, P. V. Coveney, J. Harting and F. Bresme, *Soft Matter*, 2014, **10**, 6742–6748.

47 G. B. Davies and L. Botto, *Soft Matter*, 2015, **11**, 7969–7976.

48 E. Kim, K. Stratford and M. E. Cates, *Langmuir*, 2010, **26**, 7928–7936.

49 J. M. Carmack and P. C. Millett, *Soft Matter*, 2018, **14**, 4344–4354.

50 X. Shan and H. Chen, *Phys. Rev. E: Stat. Phys., Plasmas, Fluids, Relat. Interdiscip. Top.*, 1993, **47**, 1815–1819.

51 X. Shan and G. Doolen, *J. Stat. Phys.*, 1995, **81**, 379–393.

52 U. D. Schiller and O. Kuksenok, *Reviews in Computational Chemistry*, John Wiley & Sons, Ltd, vol. 31, 2018, pp. 1–61.

53 Y. H. Qian, D. D'Humières and P. Lallemand, *Europhys. Lett.*, 1992, **17**, 479–484.

54 P. L. Bhatnagar, E. P. Gross and M. Krook, *Phys. Rev.*, 1954, **94**, 511–525.

55 X. Shan and H. Chen, *Phys. Rev. E: Stat. Phys., Plasmas, Fluids, Relat. Interdiscip. Top.*, 1994, **49**, 2941–2948.

56 X. Shan and G. Doolen, *Phys. Rev. E: Stat. Phys., Plasmas, Fluids, Relat. Interdiscip. Top.*, 1996, **54**, 3614–3620.

57 X. Shan, *Phys. Rev. E: Stat. Phys., Plasmas, Fluids, Relat. Interdiscip. Top.*, 2008, **77**, 066702.

58 A. J. C. Ladd, *Phys. Rev. Lett.*, 1993, **70**, 1339–1342.

59 A. J. C. Ladd, *J. Fluid Mech.*, 1994, **271**, 285–309.

60 A. J. C. Ladd and R. Verberg, *J. Stat. Phys.*, 2001, **104**, 1191–1251.

61 B. Dünweg and A. J. C. Ladd, *Adv. Comput. Simulat. App. Soft Matter Sci. III*, 2009, **221**, 89–166.

62 C. K. Aidun, Y. Lu and E.-J. Ding, *J. Fluid Mech.*, 1998, **373**, 287–311.

63 D. Frenkel and B. Smit, *Understanding Molecular Simulation: From Algorithms to Applications*, Academic Press, 2001.

64 S. Schmieschek and J. Harting, *Commun. Comput. Phys.*, 2011, **9**, 1165–1178.

65 F. Jansen and J. Harting, *Phys. Rev. E: Stat. Phys., Plasmas, Fluids, Relat. Interdiscip. Top.*, 2011, **83**, 046707.

66 A. J. C. Nguyen and N.-Q. Ladd, *Phys. Rev. E: Stat. Phys., Plasmas, Fluids, Relat. Interdiscip. Top.*, 2002, **66**, 046708.

67 B. J. Berne and P. Pechukas, *J. Chem. Phys.*, 1972, **56**, 4213–4216.

68 J. G. Gay and B. J. Berne, *J. Chem. Phys.*, 1981, **74**, 3316–3319.

69 G. B. Davies, T. Krüger, P. V. Coveney, J. Harting and F. Bresme, *Adv. Mater.*, 2014, **26**, 6715–6719.

70 Q. Xie, G. B. Davies and J. Harting, *ACS Nano*, 2017, **11**, 11232–11239.

71 Q. Xie and J. Harting, *Adv. Mater.*, 2021, **33**, 2006390.

72 J. Yan, M. Bloom, S. C. Bae, E. Luijten and S. Granick, *Nature*, 2012, **491**, 578–581.

73 J. Yan, S. C. Bae and S. Granick, *Soft Matter*, 2014, **11**, 147–153.

74 S. Schmieschek, L. Shamardin, S. Frijters, T. Krüger, U. D. Schiller, J. Harting and P. V. Coveney, *Comput. Phys. Commun.*, 2017, **217**, 149–161.

75 C. A. Grattoni, R. A. Dawe, C. Y. Seah and J. D. Gray, *J. Chem. Eng. Data*, 1993, **38**, 516–519.

76 S. Trevenen and P. J. Beltramo, *J. Colloid Interface Sci.*, 2021, **583**, 385–393.

77 W. Fei, M. M. Driscoll, P. M. Chaikin and K. J. M. Bishop, *Soft Matter*, 2018, **14**, 4661–4665.

78 W. Fei, P. M. Tzelios and K. J. M. Bishop, *Langmuir*, 2020, **36**, 9b03119.

79 V. Vanoli, G. Massobrio, F. Pizzetti, A. Mele, F. Rossi and F. Castiglione, *ACS Omega*, 2022, **7**, 42845–42853.

80 L. Chen, A. He, J. Zhao, Q. Kang, Z.-Y. Li, J. Carmeliet, N. Shikazono and W.-Q. Tao, *Prog. Energy Combust. Sci.*, 2022, **88**, 100968.

81 T. Lu, Y. Zhu, W. Wang and A. Wang, *J. Cleaner Prod.*, 2020, **277**, 124092.

82 A. E. Garcia, C. S. Wang, R. N. Sanderson, K. M. McDevitt, Y. Zhang, L. Valdevit, D. R. Mumm, A. Mohraz and R. Ragan, *Nanoscale Adv.*, 2019, **1**, 3870–3882.

83 V. M. Kendon, J.-C. Desplat, P. Bladon and M. E. Cates, *Phys. Rev. Lett.*, 1999, **83**, 576–579.

84 V. M. Kendon, M. E. Cates, I. Pagonabarraga, J.-C. Desplat and P. Bladon, *J. Fluid Mech.*, 2001, **440**, 147–203.

85 M. Laradji, S. Toxvaerd and O. G. Mouritsen, *Phys. Rev. Lett.*, 1996, **77**, 2253–2256.

86 M. T. Q. S. da Silva, M. do Rocio Cardoso, C. M. P. Veronese and W. Mazer, *Mater. Today: Proc.*, 2022, **58**, 1344–1349.

87 S. Cooper, A. Bertei, P. Shearing, J. Kilner and N. Brandon, *SoftwareX*, 2016, **5**, 203–210.



88 D. A. G. Bruggeman, *Ann. Phys.*, 1935, **416**, 636–664.

89 B. Tjaden, S. J. Cooper, D. J. Brett, D. Kramer and P. R. Shearing, *Curr. Opin. Chem. Eng.*, 2016, **12**, 44–51.

90 J.-W. Luo, L. Chen, T. Min, F. Shan, Q. Kang and W. Tao, *Int. J. Heat Mass Transfer*, 2020, **146**, 118837.

91 M. Reeves, A. T. Brown, A. B. Schofield, M. E. Cates and J. H. J. Thijssen, *Phys. Rev. E: Stat. Phys., Plasmas, Fluids, Relat. Interdiscip. Top.*, 2015, **92**, 032308.

92 J. A. C. Veerman and D. Frenkel, *Phys. Rev. A: At., Mol., Opt. Phys.*, 1992, **45**, 5632–5648.

93 B. J. Newton, K. A. Brakke and D. M. A. Buzzo, *Phys. Chem. Chem. Phys.*, 2014, **16**, 26051–26058.

94 A. T. Prakoso, H. Basri, D. Adanta, I. Yani, M. I. Ammarullah, I. Akbar, F. A. Ghazali, A. Syahrom and T. Kamarul, *Biomedicines*, 2023, **11**, 427.

95 H. Chen, A. Pei, J. Wan, D. Lin, R. Vilá, H. Wang, D. Mackanic, H.-G. Steinrück, W. Huang, Y. Li, A. Yang, J. Xie, Y. Wu, H. Wang and Y. Cui, *Joule*, 2020, **4**, 938–952.

96 M. Ebner, D.-W. Chung, R. E. Garca and V. Wood, *Adv. Energy Mater.*, 2014, **4**, 1301278.

97 M. A. Khan, A. J. Srockel, K. A. Macmillan, M. T. Alting, S. P. Kharal, S. Boakye-Ansah and M. F. Haase, *Adv. Mater.*, 2022, **34**, 2109547.

98 B. Kinkead, R. Malone, G. Smith, A. Pandey and M. Trifkovic, *Chem. Mater.*, 2019, **31**, 7601–7607.

99 A. Toor, T. Feng and T. P. Russell, *Eur. Phys. J. E: Soft Matter Biol. Phys.*, 2016, **39**, 57.

100 S. Shi and T. P. Russell, *Adv. Mater.*, 2018, **30**, 1800714.

101 P. Y. Kim, Y. Gao, Z. Fink, A. E. Ribbe, D. A. Hoagland and T. P. Russell, *ACS Nano*, 2022, **16**, 5496–5506.

